Contents lists available at ScienceDirect

European Journal of Pharmaceutical Sciences

Pre-miRNA-149 G-quadruplex as a molecular agent to capture nucleolin

Tiago Santos [a], André Miranda [a], Lionel Imbert [b,c], Andreia Jardim [d], Catarina R.F. Caneira [d], Virgínia Chu [d], João P. Conde [d,e], Maria Paula Cabral Campello [f,g], António Paulo [f,g], Gilmar Salgado [h], Eurico J. Cabrita [i], Carla Cruz [a,*]

[a] CICS-UBI – Centro de Investigação em Ciências da Saúde, Universidade da Beira Interior, Covilhã, Portugal
[b] Univ. Grenoble Alpes, CNRS, CEA, Institut de Biologie Structurale (IBS), Grenoble, France
[c] Univ. Grenoble Alpes, CNRS, CEA, EMBL Integrated Structural Biology Grenoble (ISBG), Grenoble, France
[d] Instituto de Engenharia de Sistemas e Computadores - Microsistemas e Nanotecnologias (INESC MN) and IN - Institute of Nanoscience and Nanotechnology, Lisbon, Portugal
[e] Department of Bioengineering, Instituto Superior Técnico, Universidade de Lisboa, Lisbon, Portugal
[f] Centro de Ciências e Tecnologias Nucleares, Instituto Superior Técnico, Universidade de Lisboa, Estrada Nacional 10 (km 1397), 2695-066 Bobadela LRS, Portugal
[g] DECN -Departamento de Engenharia e Ciências Nucleares, Instituto Superior Técnico, Universidade de Lisboa, Portugal
[h] Univ. Bordeaux, ARNA Laboratory INSERM, U1212, CNRS UMR 5320, IECB, Pessac, France
[i] UCIBIO, REQUIMTE, Faculdade de Ciências e Tecnologia, Universidade Nova de Lisboa, Caparica, Portugal

ARTICLE INFO

ABSTRACT

One of the most significant challenges in capturing and detecting biomarkers is the choice of an appropriate biomolecular receptor. Recently, RNA G-quadruplexes emerged as plausible receptors due to their ability to recognize with high-affinity proteins. Herein, we have unveiled and characterized the capability of the precursor microRNA 149 to form a G-quadruplex structure and determined the role that some ligands may have in its folding and binding capacity to nucleolin. The G-quadruplex formation was induced by K^+ ions and stabilized by ligands, as demonstrated by nuclear magnetic resonance and circular dichroism experiments. Surface plasmon resonance measurements showed a binding affinity of precursor microRNA 149 towards ligands in the micro-molar range (10^{-5}–10^{-6} M) and a strong binding affinity to nucleolin RNA-binding domains 1 and 2 (8.38 × 10^{-10} M). Even in the presence of the ligand PhenDC3, the binding remains almost identical and in the same order of magnitude (4.46 × 10^{-10} M). The molecular interactions of the RNA G-quadruplex motif found in precursor miRNA 149 (5′-GGGAGGGAGGGACGGG- 3′) and nucleolin RNA-binding domains 1 and 2 were explored by means of molecular docking and molecular dynamics studies. The results showed that RNA G-quadruplex binds to a cavity between domains 1 and 2 of the protein. Then, complex formation was also evaluated through polyacrylamide gel electrophoresis. The results suggest that precursor microRNA 149/ligands and precursor microRNA 149/nucleolin RNA-binding domains 1 and 2 form stable molecular complexes. The *in vitro* co-localization of precursor microRNA 149 and nucleolin in PC3 cells was demonstrated using confocal microscopy. Finally, a rapid and straightforward microfluidic strategy was employed to check the ability of precursor microRNA 149 to capture nucleolin RNA-binding domains 1 and 2. The results revealed that precursor microRNA 149 can capture nucleolin RNA-binding domains 1 and 2 labeled with Fluorescein 5-isothiocyanate in a concentration-dependent manner, but PhenDC3 complexation seems to decrease the ability of precursor microRNA 149 to capture the protein. Overall, our results proved the formation of the G-quadruplex structure in the precursor microRNA 149 and the ability to recognize and detect nucleolin. This proof-of-concept study could open up a new framework for developing new strategies to design improved molecular receptors for capture and detection of nucleolin in complex biological samples.

---

* Corresponding author.
  E-mail address: carlacruz@fcsaude.ubi.pt (C. Cruz).

1. Introduction

In the last few years, several studies have investigated the ability of a significant number of biomolecular agents to selectively recognize cancer biomarkers (Huang et al., 2021; Sun et al., 2016). Among the investigated bioreceptors for protein in cancer, G-quadruplex (G4) molecules seem to be promising biosensing agents (Li et al., 2016). The G4s found in RNA, can adopt a parallel topology and exhibit greater stability, which makes them more suitable to be used as biosensing agents (Kharel et al., 2020).

Precursor microRNAs (pre-miRNAs), adopting G4 structure, have been described as structures with high stability, as previously showed for pre-miRNA-149 (Kwok et al., 2016), pre-miRNA-92b (Mirihana Arachchilage et al., 2015) and pre-miRNA-26a (Liu et al., 2020). The folding of the RNA into a G4 is dependent on the presence of specific cations in solution and could be modulated by the addition of stabilizing/destabilizing small molecules (Tao et al., 2021). In the presence of K^+ ions and/or ligands that stabilize G4 formation, like pyridostatin (PDS), the pre-miRNA-149 adopts a G4 form, which prevents miRNA-149 biogenesis, and in absence of ions and ligands the biogenesis of miRNA-149 remains unaffected (Kwok et al., 2016). On the other hand, in the presence of tetra-(N-methyl-4-pyridyl)porphyrin (TMPyP4), the pre-miRNA-149 G4 is disrupted leading to a restoration of miRNA-149 biogenesis (Ghosh et al., 2019). Recently, we have characterized the RNA G4 (rG4) region of pre-miRNA 149 (5′ – GGGAGGGAGGGACGGG - 3′) and pre-miRNA 92b (5′ – GGGCGGGCGGGAGGG – 3′) and proved its high affinity and specific interaction with nucleolin (NCL) (Santos et al., 2020, 2019).

NCL is a key protein involved in several cellular functions controlling different RNA and DNA metabolism components, including ribosome biogenesis, ribosomal RNA maturation, ribosomal DNA transcription, and chromatin structure (Jia et al., 2017; Ugrinova et al., 2018). Also, it has been reported that NCL is an accessory protein in miRNA biogenesis and controls the induction of apoptosis (Pickering et al., 2011). NCL is mainly located at the cell nucleolus and nucleoplasm (Ugrinova et al., 2018), and it is also found in the cytoplasm and on the cell membrane, affecting many biological functions (Koutsioumpa and Papadimitriou, 2014). The overexpression of NCL and increased localization at the cell membrane has been shown in several cancer types (Berger et al., 2015; Hovanessian et al., 2000). Its ability to bind molecules in the surface of cancer cells associated with its capability to internalize molecules, make NCL a promisor target for the development of novel specific agents.

The G4 aptamer AS1411 has been developed for targeting nucleolin (NCL) and showed promising activity against metastatic renal cell carcinoma and acute myeloid leukemia (Bates et al., 2017; Rosenberg et al., 2014). However, in the last years has also been employed as a biosensing and bioimaging agent to selectively detect nucleolin (Miranda et al., 2021b; 2021a).

Ultrasensitive detection of NCL is of utmost importance in the diagnosis and prognosis of cancer (Chalfin et al., 2017). In the past years, several proof-of-concept tools have been designed for the detection of NCL through simple, rapid, sensitive and specific applications (Chalfin et al., 2017). Indeed, recent studies have documented the use of microfluidics to detect NCL in cancer cells based on anti-nucleolin AS1411 or locked nucleic acid (LNA) aptamers (Li et al., 2016; Maremanda et al., 2015; Miranda et al., 2021a).

In this work, we have confirmed the formation of the RNA G4 in pre-miRNA-149 and its ability to recognize NCL by different computational and experimental methods. Overall, this study could foster the development of new molecular recognition agents that specifically detect NCL.

2. Materials and methods

2.1. Bioinformatic analysis

pre-miRNA-149 sequences were obtained from miRBase version 22.1 (Kozomara and Griffiths-Jones, 2014). The human pre-miRNA-149 sequence was analysed using QGRS-mapper algorithm (Kikin et al., 2006) and G4RNA screener tool (Garant et al., 2018), which includes the scoring systems of G4Hunter (Brázda et al., 2019), cGcC (Beaudoin et al., 2014) and G4NN (Garant et al., 2017). The default parameters were applied for QGRS-mapper analysis. For G4RNA screener tool analysis, the default parameters were applied except for the size of the window that was defined to 89nt. RNA Structure prediction server (https://rna.urmc.rochester.edu/RNAstructureWeb/) was used to determine the predicted hairpin secondary structure of pre-miRNA-149. The pairwise alignment of pre-miRNA-149 sequences from several species was performed using Multiple Alignment Fast Fourier Transform (MAFFT v7 server - https://mafft.cbrc.jp/alignment/server/) with default options. The graphical alignment and conservation of the rG4 region were visualized with Jalview v2.11.1.3 software.

2.2. Oligonucleotides and ligands

All oligonucleotides were obtained from Eurofins (USA) with HPLC-grade purification. Oligonucleotide stock solutions of approximately 100 µM were prepared using DEPC water (Sigma-Aldrich, USA) and stored at −80 °C until used. Annealing of oligonucleotide sequences was performed in 20 mM phosphate buffer (10 mM KH_2PO_4, 10 mM K_2HPO_4, pH 7.1) supplemented with 100 mM KCl by heating the samples for 10 min at 95 °C and cooling on ice for 30 min before the experiments. Synthesis and purification of the ligands 10-(8-(4-iodobenzamide) octyl))−3,6-bis(dimethylamine) acridinium iodide (C_8) and 10-(8-(4-iodobenzamide)octyl))−3,6-bis(dimethylamine) acridinium (C_8−NH_2) were performed as previously described (Pereira et al., 2017). 3,3′-[1, 10-Phenanthroline-2,9-diylbis(carbonylimino)]bis[1-methyl-quinolinium] 1,1,1-trifluoromethanesulfonate (PhenDC3) was obtained from Sigma-Aldrich (USA). The chemical structures of each ligand are depicted in Fig. 1A. Stock solutions of the compounds were prepared as 10 mM solutions in DMSO (Thermo Fisher Scientific, USA) and their subsequent dilution was done using nuclease-free water. Fluorescein 5-isothiocyanate (FITC) was also purchased from Sigma-Aldrich (USA).

2.3. Cloning, cell-free expression and purification

The sequence corresponding to NCL RNA binding domains 1 and 2 (NCL RBD1,2) was cloned into a pIVEX 2.4D vector. NCL RBD1,2 was synthesized *in vitro* using a cell-free expression system (Imbert et al., 2021). Briefly, NCL RBD1,2 was expressed in a volume of 9 mL under RNAse-free conditions in dialysis mode, with 1/10 ratio of the reaction mixture to feeding mixture for 16 h at 23 °C under gentle agitation. The cell-free mixture contained 16 µg/mL of pIVEX 2.4D plasmid encoding the NCL RBD1,2 sequence, 1 mM of each essential amino acid, 0.8 mM of each rNTPs (guanosine-, uracil-, and cytidine-5′-triphosphate), 55 mM HEPES (pH 7.5), 68 µM folinic acid, 0.64 mM cyclic adenosine monophosphate, 3.4 mM dithiothreitol, 27.5 mM ammonium acetate, 2 mM spermidine, 80 mM creatine phosphate, 208 mM potassium glutamate, 16 mM magnesium acetate, 250 µg/mL creatine kinase, 27 µg/mL T7 RNA polymerase, 0.175 µg/mL tRNA, and 400 µL/mL S30 *E. coli* bacterial extract. After incubation, the reaction mixture was diluted in binding buffer (50 mM HEPES (pH 7.5), 300 mM NaCl, and 10 mM imidazole) to a final volume of 45 mL and centrifuged for 45 min at 36, 000 g at 4 °C. Thereafter, the supernatant was applied onto a 5 mL Ni-NTA column that had been previously equilibrated in binding buffer at 4 °C. The column was washed with 5% of elution buffer (50 mM HEPES (pH 7.5), 300 mM NaCl, and 500 mM imidazole) to eliminate residual contaminants and the protein was eluted with 50% of elution
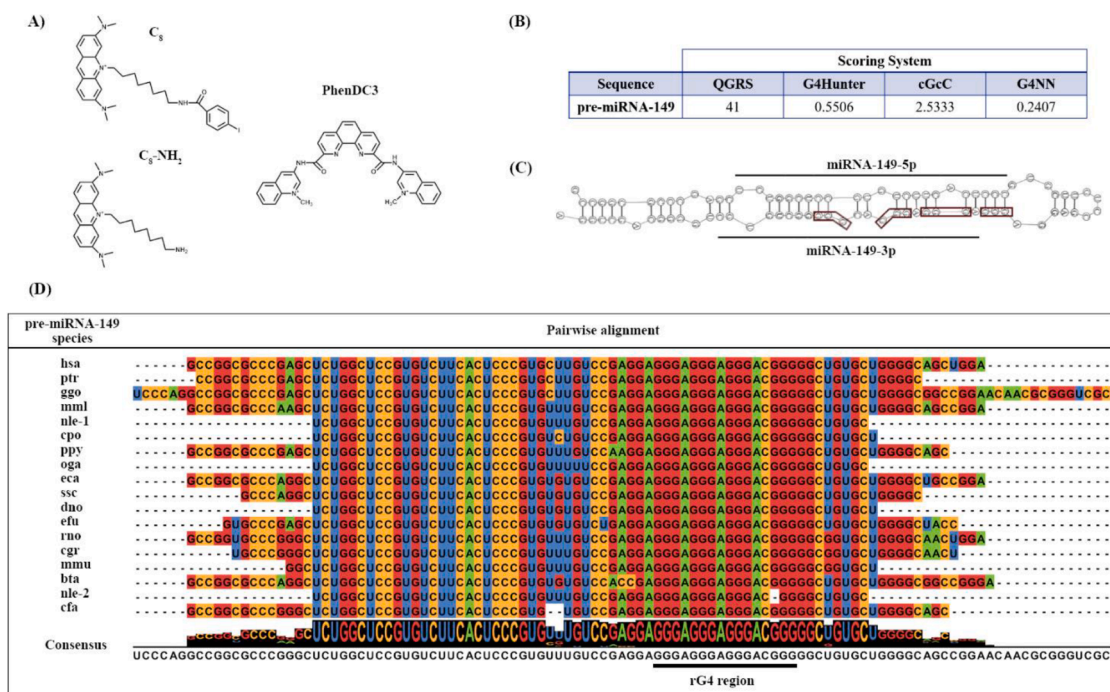
Fig. 1. (A) Chemical structures of C_8, C_8–NH_2 and PhenDC3. (B) G4 scores of pre-miRNA-149 predicted by using QGRS-Mapper, G4Hunter, cGcC and G4NN. (C) Predicted secondary structure of pre-miRNA-149 showing miRNA-149–5p, miRNA-149–3p and the rG4 region. (D) Pairwise alignment and conservation of pre-miRNA-149 sequences found in several species.

buffer. Fraction containing the NCL RBD1,2 was pooled and concentrated on a 10-kDa cut-off membrane. The purity of each fraction was analyzed by sodium dodecyl sulfate polyacrylamide gel electrophoresis (SDS-PAGE) and the protein was identified through western blot analysis using the primary anti-NCL antibody (Thermo Fisher, ref. PA3–16875).

2.4. NMR spectroscopy

Standard ^1H NMR spectra with water suppression using excitation sculpting (acquired with zgesgp pulse program from the Bruker pulse program library) were acquired on a 600 MHz Bruker Avance III spectrometer with a QCI cryoprobe. Pre-miRNA-149 was used at a concentration of approximately 20 μM with a total volume of 200 μL in a 3 mm NMR tube, annealed as described above and supplemented with 10% D_2O (Eurisotop, France). The spectrum was acquired and processed with the software Topspin 3.1. Figures were prepared using TopSpin 4.0.6. Chemical shifts (δ) are reported in ppm.

2.5. Circular dichroism

CD spectra were acquired in a Jasco J-815 spectrometer (Jasco, USA), using a Peltier temperature controller (model CDF-426S/15). pre-miRNA-149 sequence was annealed as previously described. Unless otherwise stated, a 1 mm path-length quartz cuvette (Hellma, Germany) was used with pre-miRNA-149 at 10 μM in 20 mM lithium cacodylate buffer (Sigma-Aldrich, USA) at pH 7.2, supplemented with KCl (Thermo Fisher Scientific, USA). The required volume for the titrations was added directly to the quartz cell. The CD melting experiments were performed in the temperature range of 20–100 °C, with a heating rate of 2 °C/min by monitoring the ellipticity at 262 nm. Spectra acquisition was performed in the absence and presence of increasing concentrations of KCl or ligands. Data was converted into fraction folded (f) plots.

$$f = \frac{CD - CD_\lambda^{min}}{CD_\lambda^{max} - CD_\lambda^{min}} \qquad (1)$$

Data points were then fitted to a Boltzmann or bi-dose response distribution equations (OriginPro 2016) and the melting temperatures were determined.

2.6. Molecular docking and molecular dynamics simulations

The minimized model of the rG4 found in pre-miRNA-149 (5′-GGGAGGGAGGGACGGG- 3) was recently built and described by some of us (Carvalho et al., 2020), was used as a target for molecular docking studies. The rG4 structure and the NCL RBD1,2 (PDB: 2KRR) solution structure were optimized for docking using the Dock Prep tool of Chimera 1.15. After assigning polar hydrogens and Gasteiger charges, docking simulations were carried with AutoDock 4.2.6 program using Lamarckian genetic algorithm. The size of the box was constrained to $100 \times 100 \times 100$ Å along the x, y, and z axes, respectively, with a grid spacing of 0.375 Å. A total of 10 runs were performed with an initial population of 150 random individuals, a maximum number of evaluations set to 2.5×10^7, the rate of mutation and crossover set to 0.02 and 0.8, respectively, and an elitism value of 1. The most representative structures were selected based on the binding free energy and further processed with MD simulations the all-atom force field AMBER99SB of GROMACS 2020.6 package. For MD simulations, the rG4/NCL RBD1,2 complex was centered in an octahedral box and solvated with TIP3P water molecules and K^+ atoms to neutralize the system. After an energy minimization of 1000 steps using the steepest descent algorithm, the system was gradually heated to 300 K in 100 ps under the control of Berendsen thermostat followed by 100 ps isobaric simulation under the control of the Parrinello-Rahman barostat. Finally, explicit solvent MD runs of 100 ns were performed for rG4/NCL RBD1,2 complex at constant temperature (300 K) and pressure (1 atm). The Particle mesh Ewald (PME) method was used for calculating long-range electrostatic interactions. A 1 nm cut-off was applied to short-range Lennard-Jones interactions. Coordinates were collected in trajectory files every 10 ps. All molecular images were rendered using UCSF ChimeraX. 2D diagrams of G4/NCL RBD1,2 complex were determined by using LigPlot+ v.2.2.4.

2.7. Non-denaturing polyacrylamide gel electrophoresis

Non-denaturing polyacrylamide gel (15%) electrophoresis was used to visualize the oligonucleotides. pre-miRNA-149 samples were prepared at a concentration of approximately 1 μM. Sucrose (Sigma-Aldrich, USA) was added to the samples at a final concentration of 23%. Oligonucleotide marker was loaded in parallel on the gel. The pre-miRNA-149 sequence was injected with and without KCl. A molar ratio of 1:1 of pre-miRNA-149/ligand and pre-miRNA-149/NCL RBD1,2 was prepared and the mixture was incubated for 30 min. The supra-molecular complexes of pre-miRNA-149/ligand/NCL RBD1,2 were prepared at a molar ratio of 1:1:1. Electrophoresis was performed at 2 W per gel to reach a temperature close to 20 °C. After electrophoresis, the gel was stained by Stains-All solution (Sigma-Aldrich, USA) for 30 min under gentle agitation. Thereafter, the gel was incubated for 2 h in water for discolouration under the light before visualization.

2.8. Surface plasmon resonance (SPR)

All SPR measurements were carried out on a Biacore T200 (Biacore, GE Healthcare, Sweden) with a SA (streptavidin-coated sensor chip) sensor chip (GE Healthcare, Sweden). The biotin-labeled pre-miRNA-149 sequence (25 nM) was dissolved in 20 mM phosphate buffer (10 mM KH_2PO_4, 10 mM K_2HPO_4, pH 7.1) supplemented with 100 mM KCl and annealed as above described. Meanwhile, the sensor chip was equilibrated with running buffer at 25 μL/min for 1 h. Activation buffer (1 M NaCl, 50 mM NaOH) was injected for 3 min seven times to remove unbound streptavidin from the sensor chip. After that, in order to ensure surface stability, two primes with running buffer were performed and the buffer was flowed for 10 min at a flow rate of 1 μL/min. Manual inject was used to immobilize biotin-labeled pre-miRNA-149 on flow cell 2 (100 μL of a 25 nM pre-miRNA-149) and the injection was stopped after the desired level was reached ($\sim$ 250 RU to minimize mass transport effects). Flow cell 1 was used as a control and is left blank for subtraction.

For kinetic/affinity analysis, each ligand and NCL RBD1,2 were serially diluted in running buffer. All experiments were performed in triplicate at 25 °C. Each ligand and NCL RBD1,2 were injected from low to high concentrations during 75 s with a flow rate of 50 μL/min, followed by dissociation of 600 s. Surface regeneration was achieved by injecting two pulses of 30 s of 10 mM glycine/HCl pH 2.5, and the next three 60 s injections of running buffer to remove any trace of regeneration solution.

BiaEvaluation Software was used for data analysis and the likelihood of fittings was assessed through the statistical parameters of Chi^2 and U-value. All sensorgrams were double corrected for non-specific binding and refractive index changes (bulk effect) by subtracting the signals of an equivalent injection across the reference flow cell 1. The equilibrium dissociation constant K_D was obtained by plotting the response at equilibrium (Req) *versus* the analyte concentration and then fitted as a Langmuir isotherm:

$$Req = \frac{[Analyte]Rmax}{K_D + [Analyte]} + RI$$

Rmax is the analyte binding capacity and RI is the bulk refractive index contribution of the sample, which is assumed to be the same for all the injections and used as the Response-axis offset.

2.9. Fluorescein isothiocyanate (FITC) labeling

FITC was used to attach a fluorescent label to NCL RBD1,2 via the amine group. The isothiocyanate group reacts with amino terminal and primary amines in NCL RBD1,2. Briefly, 2 mg/mL of NCL RBD1,2 was dissolved in 0.1 M sodium bicarbonate buffer (pH 8.3). Then, FITC dissolved in DMSO (10 mg/mL) was added to the solution. The reaction mixture was incubated for 4 h with continuous stirring. To remove the unbounded FITC, the mixture was washed on a 10-kDa cut-off membrane.

The labeling of pre-miRNA-149 with the FITC dye was performed using 100 μg of pre-miRNA-149. The mixture was added to 71 μL of labeling buffer (0.020 g of sodium (di)tetraborate in 1 mL of H2O) and 2 μL of FITC (100 mg of FITC in 200 μL of sterile DMSO). Thereafter, the solution was stirred for 4 h at RT, protected from light. Finally, pre-miRNA-149 was incubated with 3 M NaCl and 2.5 vol of absolute ethanol and incubated overnight at −20 °C. Excess FITC was removed by centrifugation at 12,000 g for 30 min at 4 °C. After centrifuging, the pellet was washed with 75% ethanol twice, followed by a 5 min centrifugation at 12,000 g (4 °C).

2.10. Confocal microscopy

PC3 cell line was grown in RPMI medium supplemented with 10% (v/v) FBS and 1% (v/v) penicillin-streptomycin. Cultures were maintained in a humidified chamber at 37 °C and 5% CO2. Cells were subsequently harvested and seeded in μ-Slide 8-well flat bottom imaging plates (Ibidi GmbH, Germany) at a plating density of 5 $\times 10^4$ cells/well and incubated for cell attachment for 24 h at 37 °C and 5% CO_2. Thereafter, cells were incubated with the primary anti-NCL polyclonal antibody (Thermo Scientific, USA) for 2 h at 37 °C. Following primary antibody incubation, cells were washed 3 $\times$ with fresh serum-free medium and incubated with secondary antibody anti-rabbit IgG conjugated with Alexa Fluor® 647 (Thermo Scientific, USA) for 1 h at 37 °C. Thereafter, cells were washed 3 $\times$ with fresh serum-free medium and stained with Hoechst 33,342® nuclear probe (1 μM) for 10 min. Subsequently, the cells were incubated with pre-miRNA-149 (10 μM) labeled with FITC and incubated for 12 h at 37 °C and 5% CO_2. Thereafter, the cells were transferred to a Zeiss LSM 710 confocal laser scanning microscope (CLSM; Carl Zeiss SMT Inc., USA) equipped with a plane-apochromat 63 $\times$ /DIC objective and processed in Zeiss Zen (SP2, 2010), in order to evaluate the cellular uptake. The fluorescence images were obtained at 63 $\times$ magnification.

2.11. Microfluidic experiments

Polydimethylsiloxane (PDMS) microfluidic devices were fabricated using standard mold replication techniques, as previously described (Pinto et al., 2017). The device was designed to have two-channel heights to allow the holding of the beads inside the channel. The packing of streptavidin beads was carried out as previously detailed (Pinto et al., 2017). Briefly, the liquids were driven inside the microchannel using a syringe pump exerting a negative pressure at the outlet (NE-1002X, New Era Pump System Inc., USA). The beads were first suspended in a solution of 20% (w/w) polyethylene glycol 8000 (PEG) (Sigma-Aldrich, USA) and packed inside the channel at a flow rate of 7 μL/min, followed by a washing step with 20 mM phosphate buffer (10 mM KH_2PO_4, 10 mM K_2HPO_4, pH 7.1) supplemented with 100 mM KCl at a flow rate of 7 μL/min.

Thereafter, the pre-miRNA-149 (5 μM) was incubated with PhenDC3 at 1 molar equivalents during 10 min. After that, different concentrations of NCL RBD1,2 labeled with FITC were added and incubated for 30 min. The experiment was carried out at a flow rate of 1 μL/min for 30 min. Finally, the channels were washed with 20 mM phosphate buffer (10 mM KH_2PO_4, 10 mM K_2HPO_4, pH 7.1) supplemented with 100 mM KCl at a flow rate of 5 μL/min for 2 min to remove non-specifically bound molecules. All fluorescence images were acquired with an exposure time of 2 s in an Axio Imager Z2 microscope using 579 nm as the excitation wavelength (BP 565/30) and collecting the emission at 591 nm (BP 620/60) and processed in Zeiss Zen Software (SP2, 2010) and ImageJ (National Institute of Health, USA). Fluorescence emission values were obtained by averaging the entire end-section of the microcolumns. For every individual experiment, new structures with fresh functionalization steps were performed. ImageJ was used to analyze the

fluorescence images.

3. Results

3.1. Bioinformatic analysis of pre-miRNA-149 G4

The ability of pre-miRNA-149 to adopt a G4 structure was investigated by means of an *in silico* approach using the QGRS-mapper algorithm (Kikin et al., 2006) and the G4RNA screener tool (Garant et al., 2018), which includes the scoring systems of G4Hunter (Brázda et al., 2019), cGcC (Beaudoin et al., 2014) and G4NN (Garant et al., 2017). The results highlighted G4 scores of 41, 0.5506, 2.5333 and 0.2407 for QGRS-mapper, G4Hunter, cGcC and G4NN, respectively (Fig. 1B). The G4 sequence in pre-miRNA-149 (Fig. 1C) identified by the QGRS-mapper algorithm was 5′-GGGAGGGAGGGACGGG-3′. Next, the conservation of the G4 sequence in several species was evaluated by a pairwise alignment of pre-miRNA-149 sequences using Multiple Alignment Fast Fourier Transform (MAFFT v7 server - https://mafft.cbrc.jp/alignment/server/). The results showed that the rG4 region of pre-miRNA-149 is highly conserved among the different species (Fig. 1D).

3.2. pre-miRNA-149 G4 formation

The ability of pre-miRNA-149 to form a G4 structure in the presence of K^+ was assessed by means of 1D ^{1}H NMR spectroscopy and CD measurements (Fig. 2). As seen in Fig. 2A, the ^{1}H NMR spectrum revealed proton resonances in both the G4 (10–12 ppm) and Watson--Crick (12–14.5 ppm) regions. The resonances in the Watson-Crick region are sharp and well resolved, while we observe intense overlapped signals in the G4 imino proton region. Therefore, in order to assess the formation and stability of the G4 form by pre-miRNA-149, we performed CD measurements to optimize the annealing of the G4 structure. The results depicted in Fig. 2B showed that upon increasing temperature to 95 °C and cooling the sample in ice, the positive band with maximum ellipticity at 265 nm exhibits a slight shift to 261 nm. The structure also remains stable throughout 24 h and 48 h of incubation at 4 °C.

3.3. Evaluation of K^+ dependence in the formation of pre-miRNA-149 G4

CD measurements of the pre-miRNA-149 in the absence and presence of increasing amounts of KCl were performed to further check the influence of K^+ ions in the formation of the G4 structure by pre-miRNA-149. As seen in Fig. 3A, upon titration with KCl of the pre-miRNA-149 solution, a noticeable increase in the band intensity was observed after addition of 10 mM KCl. The CD profile was conserved and is characteristic of a parallel G4 topology. In fact, it is possible to notice that the band intensity is K^+ dependent. These K^+-dependent amplitude changes in CD bands are indicative of G4 formation. In order to investigate the thermal stability of pre-miRNA-149 in the presence of K^+, CD melting experiments were carried out. As expected, and highlighted in Fig. 3B and **Table S1**, upon titration with increasing amounts of KCl, the thermal stability of pre-miRNA-149 increases from 57.6 ± 0.2 °C to 76.4 ± 1.3 °C in the absence and the presence of 20 mM KCl, respectively. In the presence of 50 mM and 100 mM of KCl, the melting curves could not be fitted by the Boltzmann equation due to high thermal stabilization.

3.4. Effect of G4 ligands on pre-miRNA-149 stability

The (de)stabilization of the G4 formed by pre-miRNA-149 could be significantly modulated by using ligands that decrease or increase the partially folded states of the G4 structure. Herein, we studied the effect of acridine orange (C_8 and C_8–NH_2) and phenanthroline (PhenDC3) derivatives on pre-miRNA-149. The influence of these ligands on the G4 structure and stability was investigated using CD titrations and CD melting experiments, respectively. The results revealed important findings and are highlighted in Fig. 4. The increase in the band intensity was more prominent in C_8 (Fig. 4A) and PhenDC3 (Fig. 4C) ligands. C_8–NH_2 (Fig. 4B) also demonstrated an increase in the band intensity but less prominent.

CD melting experiments were conducted in order to quantify the thermal stabilization of pre-miRNA-149 by ligands (Fig. 4D–E and supplementary **Table S2**). The results agree with those observed in CD titration experiments. The initial melting temperature of pre-miRNA-149 in the presence of 20 mM lithium cacodylate buffer supplemented with 1 mM KCl was 61.9 ± 0.2 °C. Upon addition of 2 molar equivalents of C_8–NH_2, the melting temperature was only 63.4 ± 0.4 °C. In the presence of 2 molar equivalents of C_8, the signature of melting curves suggests the presence of two pre-miRNA-149 species, since two distinct melting points were obtained from data ($T_m^1 = 64.5 ± 1.9$ °C and $T_m^2 = 96.3 ± 2.5$ °C). In the presence of 2 molar equivalents of PhenDC3, the melting temperature decreased to 58.9 ± 0.6 °C.

3.5. In silico analysis of the interaction between NCL RBD1,2 and G4 motif found in pre-miRNA-149

The interaction of the rG4 found in pre-miRNA-149 (5′-GGGAGG-GAGGGACGGG- 3′) with NCL RBD1,2 was assessed by molecular docking and molecular dynamics (MD) simulations. Recently, some of us described the predicted model of the G4 structure (Carvalho et al.,
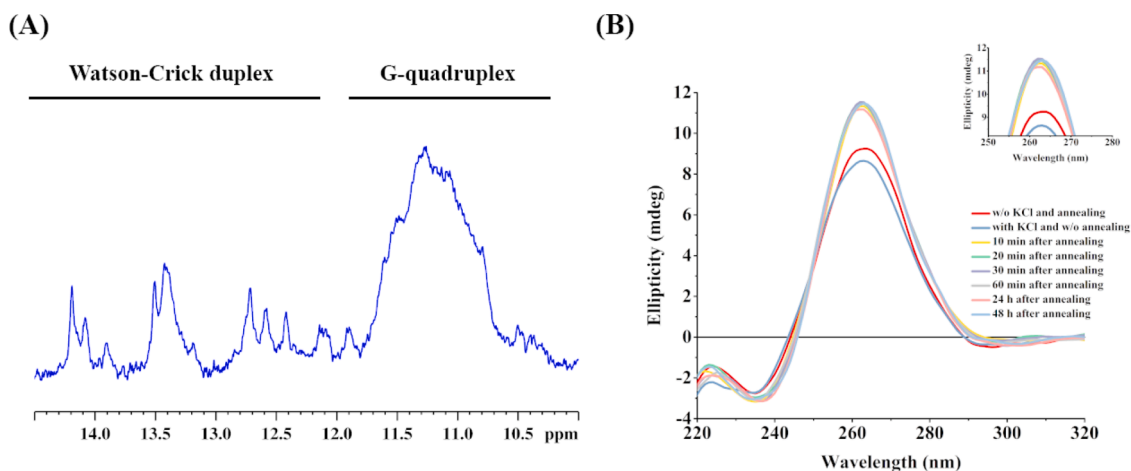

Fig. 2. (A) 1D ^{1}H spectra of pre-miRNA-149 in the presence of K^+ showing the Watson-Crick and G4 regions. (B) CD spectra of pre-miRNA-149 before and after annealing and in the absence and presence of K^+. Inset: Zoom of the maximum positive band.
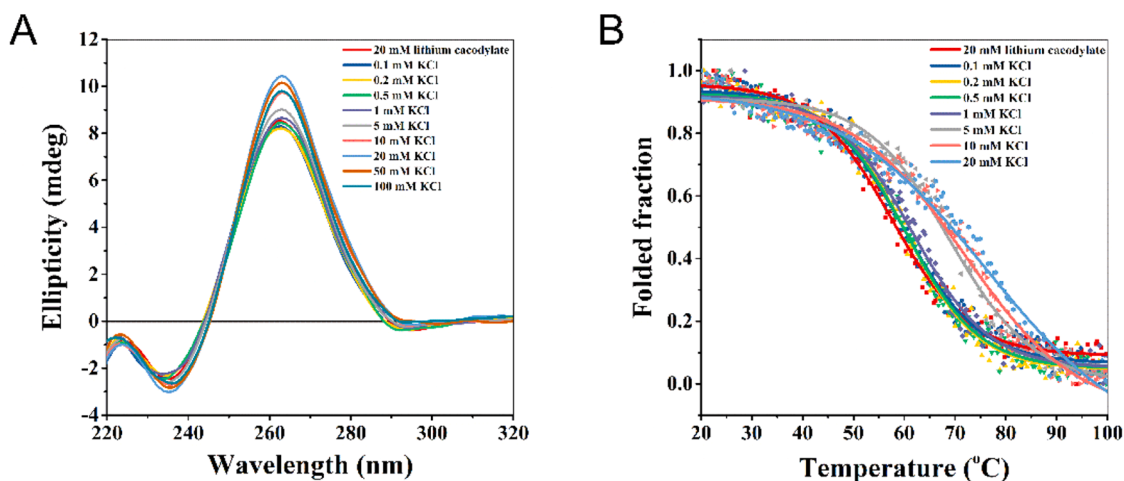
Fig. 3. (A) CD spectra of pre-miRNA-149 in 20 mM lithium cacodylate buffer in the absence and presence of increasing concentrations of KCl. (B) CD melting curves at 10 μM in the absence and presence of increasing concentrations of KCl. Data points were recorded at 262 nm.
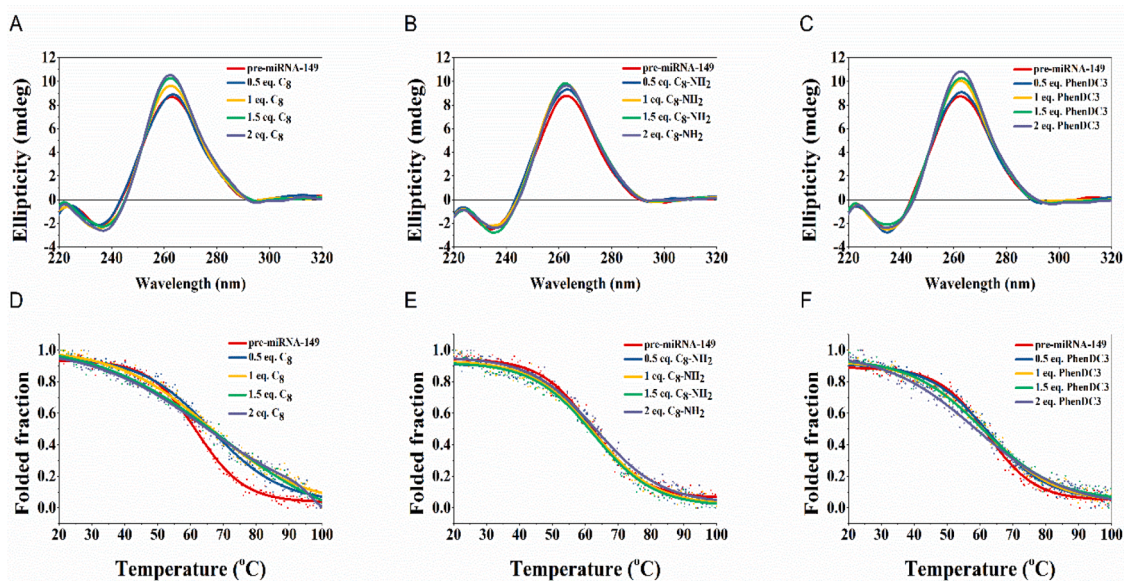

Fig. 4. (A) CD spectra of pre-miRNA-149 in 20 mM lithium cacodylate and 1 mM KCl in the absence and presence of increasing concentrations of (A) C_8, (B) C_8–NH_2 and (C) PhenDC3. CD melting normalized curves at 10 μM in the absence and presence of increasing concentrations of (D) C_8; (E) C_8–NH_2 and (F) PhenDC3. Data points were recorded at 262 nm.

2020). Considering that the solution structure of the full-length NCL remains unknown, we have used the available solution structure of NCL RBD1,2 (PDB: 2KRR) for the *in silico* analysis. The best docking conformer in terms of the lowest free binding energy was used to perform the molecular dynamics studies. The complex G4/NCL RBD1,2 after 100 ns simulation was depicted in Fig. 5A (side and top view). MD simulations showed that rG4 structure binds to NCL RBD1,2 in the binding cavity between RBD1 and RBD2. Fig. 5B shows the RMSD fluctuations of the G4/protein, protein, and G4 for complex G4/NCL RBD1,2. The visual analysis of the trajectories proved that the structures were stable throughout the simulation (100 ns). Although an initially, noticeable, RMSD fluctuation of the G4/protein and protein, the RMSD value seems to stabilize after 40 ns of simulation. Additionally, intermolecular hydrogen bonding is one of the main driving forces contributing to macromolecule and ligand binding. Hydrogen bonds observed between NCL RBD1,2 and G4 structure are shown in supplementary **Table S3**. Notably, most G4 residues act as hydrogen acceptors in the intermolecular hydrogen bonds except A4 and G5 residues, which act as hydrogen donors (Fig. 5C).

3.6. Evaluation of the formation of the pre-miRNA-149/ligand, pre-miRNA-149/NCL and pre-miRNA-149/ligand/NCL molecular complexes

The complex formation of the pre-miRNA-149 and pre-miRNA-149/ligands with NCL was determined by PAGE (Fig. 6). The oligonucleotides were diluted to 1 μM in 20 mM phosphate buffer, in the presence and absence of 100 mM KCl. The complex with ligands/NCL was prepared in a 1:1 ratio. The gel showed an intense band in the presence of 20 mM phosphate buffer, suggesting a major dominant folding form in solution (lane 1). Since the samples were annealed before their loading on the gel, it is possible that the annealing could have promoted the formation of the G4 structure with 20 mM phosphate buffer. In the presence of 100 mM KCl, the pre-miRNA-149 seems to adopt the same electrophoretic profile as in the presence of 20 mM phosphate buffer (Fig. 6A, lane 2). Considering these results, we proposed that the dominant folding form in solution could be the G4 form of pre-miRNA-149. Thereafter, to evaluate the effect of the ligands in pre-miRNA-149 molecularity, we incubated the pre-miRNA-149 sequence with ligands. The results revealed that pre-miRNA-149 in the presence of the ligands
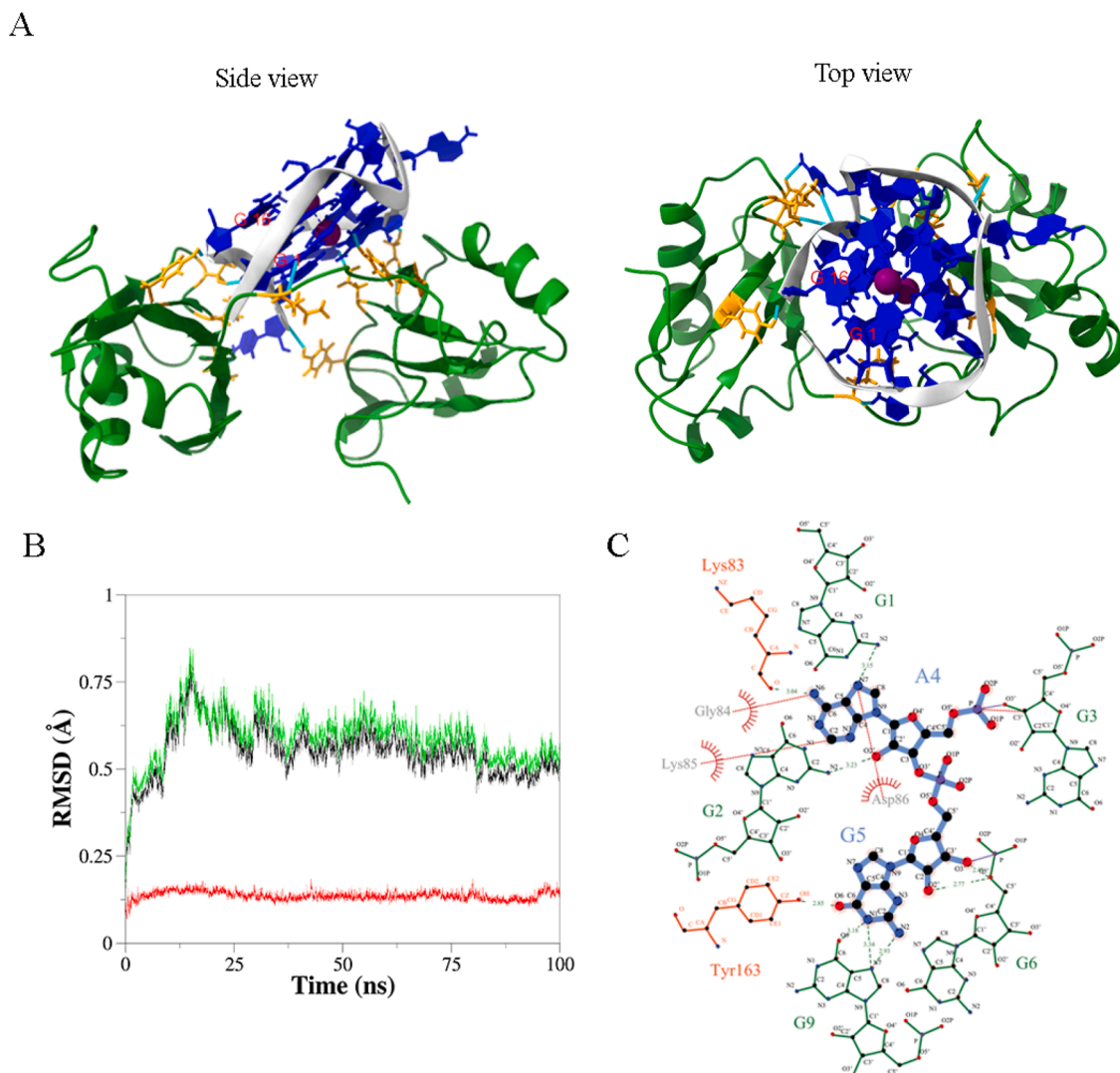
A

Side view

Top view

B

C

Fig. 5. *In silico* analysis of G4/NCL RBD1,2 complex. (A) Final snapshots of side and top view of the G4/NCL RBD1,2 complex after 100 ns MD production. G4 structure is depicted in blue with the backbone in light gray. K^+ cations are depicted as purple spheres. NCL RBD1,2 is represented in green and contact residues of the protein are highlighted in orange. H-bonds are shown in cyan, while labels are shown in red. (B) RMSD plot of the G4/protein (green), protein (black), and G4 (red) for complex G4/NCL RBD1,2. (C) Ligplot + image showing site-specific hydrogen bonding and hydrophobic interactions of NCL RBD1,2 residues and rG4 residues A4 and G5. Hydrogen bonds are depicted in dashed green lines and hydrophobic interactions in red.

retains its initial molecularity (Fig. 6A, lanes 3,4 and 5), which corroborates that the dominant folding form in solution is the G4 form. Upon addition of NCL RBD1,2, it is worth noticing that the band corresponding to pre-miRNA-149 was less intense (Fig. 6B, lane 2), suggesting the binding of almost all pre-miRNA-149 G4 to NCL RBD1,2. An intense band corresponding to the complex pre-miRNA-149/NCL RBD1,2 was visible at the high molecular weight. A similar electrophoretic profile of pre-miRNA-149 was observed in the presence of G4 ligands and NCL RBD1,2 (Fig. 6B, lanes 3,4 and 5).

3.7. Binding affinity of pre-miRNA-149 and pre-miRNA-149/ligand complexes towards NCL RBD1,2

SPR biosensor was used to investigate the interaction of pre-miRNA-149 and ligands and the binding affinity of pre-miRNA-149 or pre-miRNA-149/ligands towards NCL RBD1,2. Streptavidin sensor chips were used to capture biotin-labeled pre-miRNA-149. The SPR signal responses related to the specific interaction with the pre-miRNA-149 were obtained after subtraction of the signals recorded on the reference flow-cell as well as the running buffer injection by applying a

double referencing procedure. The binding curves demonstrated a fast association phase and a slow dissociation, which made it necessary to include glycine pH 2.5 regeneration steps. Thereafter, the SPR signals returned to the baseline. The K_D was obtained by fitting the steady-state response *vs.* the analyte concentration by Langmuir isotherm according to a 1:1 binding stoichiometry (supplementary **Fig. S1**). The values are depicted in Table 1. For all ligands, the binding affinities were in the concentration range 10^{-5}–10^{-6} M. On the other hand, the binding affinities of pre-miRNA-149 and pre-miRNA-149/NCL RBD1,2 were 8.38 $\times 10^{-10}$ M and 4.46 $\times 10^{-10}$ M, respectively.

3.8. Co-localization of NCL with pre-miRNA-149 in cancer cells

Once the binding affinity and influence of the G4 ligands have been characterized, the recognition of NCL by pre-miRNA-149, labeled with FITC, was performed in a cellular context via confocal microscopy. Nuclei are stained with Hoechst 33,342® and are displayed in blue. The primary anti-NCL antibody conjugated with the secondary antibody AlexaFluor 647® (red) was used to localize cell surface NCL. Pre-miRNA-149 was labeled with FITC (green) to allow its location in
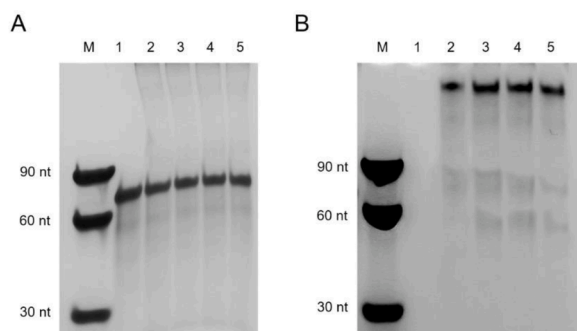
Fig. 6. PAGE under native conditions of pre-miRNA-149 in (A) absence (Lane M - migration marker; lane 1 – pre-miRNA-149 in the presence of 20 mM K_2HPO_4/KH_2PO_4; lane 2 – pre-miRNA-149 in the presence of 20 mM K_2HPO_4/KH_2PO_4 supplemented with 100 mM KCl; lanes 3 to 5 – pre-miRNA-149/ligand complexes (with 1 molar eq. of C_8, $C_8–NH_2$ and PhenDC3, respectively) and in the (B) presence of NCL RBD1,2 (1 μM) (Lane M - migration marker; lane 1 – NCL RBD1,2 (1 μM); lane 2 – pre-miRNA-149 in the presence of 20 mM K_2HPO_4/KH_2PO_4 supplemented with 100 mM KCl; lanes 3 to 5 – pre-miRNA-149/ligand complexes (with 1 molar eq. of C_8, $C_8–NH_2$ and PhenDC3, respectively). The gel was supplemented with 10 mM KCl. Migration markers were oligothymidylate single-stranded DNA ($n = 30$, 60 and 90).

Table 1
K_D (M) constant values of pre-miRNA-149 measured by SPR biosensor and obtained by the Langmuir isotherm.

Ligand	K_D (M)
C_8	9.29×10^{-6}
$C_8^-NH_2$	1.12×10^{-5}
PhenDC3	7.94×10^{-6}
NCL RBD1,2	8.38×10^{-10}
PhenDC3/NCL RBD1,2	4.46×10^{-10}

cancer cells. As depicted by Fig. 7, pre-miRNA-149 was able to co-localize with NCL-positive regions. The cytoplasm and surface of the cells in the merged image were depicted in orange, which means the merge of red and green colors from anti-nucleolin antibody and pre-miRNA-149-FITC, respectively. In addition, inside some cells, we found free pre-miRNA-149, which probably means the internalization of pre-miRNA-149 and its release from nucleolin inside the cell. These promisor results confirmed the potential of pre-miRNA-149 G4 as a molecular recognition agent to detect cell surface NCL in cancer cells.

3.9. Capture of NCL RBD1,2 by a pre-miRNA-149-based microfluidic platform

In order to confirm the ability of pre-miRNA-149 to capture NCL RBD1,2, we have used a microfluidic platform that allows the capture and fluorescence detection of NCL RBD1,2. The microfluidic assay was carried out with the pre-miRNA-149 G4, modified in 5′ end with biotin, previously annealed, and immobilized in streptavidin sepharose beads. The approach is similar to that performed in SPR biosensor. The streptavidin beads with pre-miRNA-149 G4 immobilized were flowed through the microfluidic platform and due to a biophysical entrapment were confined into the microchannel. In order to detect the NCL RBD1,2 captured by pre-miRNA-149, the protein was labeled with FITC and was injected into the microchannel at different concentrations (0.25, 0.5, 1.25, 2.5 and 5 μM). The results shown in Fig. 8 demonstrated that NCL RBD1,2 was detected in a concentration-dependent manner.

4. Discussion

Human pre-miRNA-149 was previously characterized as a G4-forming molecule and since then has been taking the attention of the researchers due to its capability to regulate miRNA biogenesis and to target G4-binding proteins (Ghosh et al., 2019; Kwok et al., 2016). Recently, using different experimental techniques we have characterized the G4 sequence (5′-GGGAGGGAGGGACGGG-3′) found in pre-miRNA-149 (Santos et al., 2019). However, in biological context, the adjacent nucleotides of a given G4 sequence can have a tremendous impact on G4 formation, since G-richness (the fraction of guanines in the sequence) and G-skewness (G/C asymmetry between the complementary nucleic acid strands) are important parameters for the *in vivo* formation of G4 structures (Klimentova et al., 2020; Santos et al., 2021).
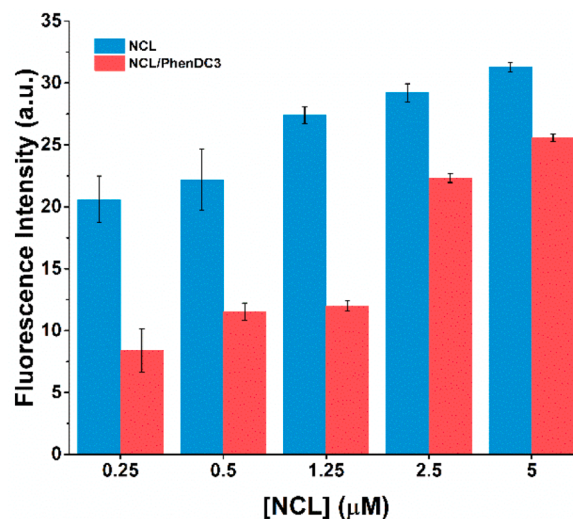

Fig. 8. Fluorescence intensity of NCL RBD1,2 labeled with FITC and captured by pre-miRNA-149 or pre-miRNA-149/PhenDC3 complex immobilized in streptavidin beads. Different concentrations of protein were flowed through the microfluidic channel (0.25, 0.5, 1.25, 2.5 and 5 μM).
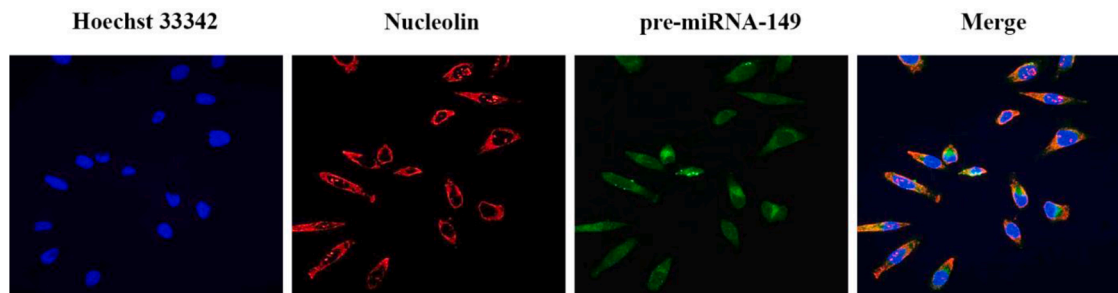

Fig. 7. Confocal microscopy images showing co-localization of NCL and pre-miRNA-149, labeled with FITC. The images showed the cells with nuclear staining by Hoechst 33,342® (1 μM, blue); pre-miRNA-149 labeled with FITC (10 μM, green); and NCL (red). NCL was labeled with the primary anti-NCL polyclonal antibody (1:100) and detected with the secondary antibody against IgG conjugated with Alexa Fluor® 647 (1:1000).

Therefore, in this work, we have characterized the pre-miRNA-149 sequence and the binding and capture of NCL.

Firstly, using an *in silico* approach, we demonstrated the formation of a G4 structure by pre-miRNA-149. The results of QGRS-mapper algorithm revealed the formation of a G4 structure in the sequence 5′-GGGAGGGAGGGACGGG-3′, which was previously characterized experimentally as a G4-forming sequence (Santos et al., 2019). This G4 oligonucleotide showed important biological capabilities and its location in the pre-miRNA-149 sequence suggests a significant post-transcriptional regulatory role in gene expression, since overlaps with miRNA-149–3p, an important antitumor miRNA in several types of cancer (He et al., 2018; Shen et al., 2020; Yang et al., 2017). On the other hand, the results from computational algorithms G4Hunter, cGcC and G4NN showed low susceptibility of the pre-miRNA-149 sequence to adopt a G4 structure. Despite these computational predictions, an initial study of Kwok et al. experimentally demonstrated the formation of the G4 structure by pre-miRNA-149 sequence through a method called SHALiPE, which is derived from the SHAPE method and consists of the coupling of selective 2′-hydroxyl acylation with a lithium ion-based primer extension (Kwok et al., 2016). Therefore, it is important to perform a deeply experimental characterization using different techniques to undoubtedly prove the G4 formation by pre-miRNA-149.

The results from conservation studies also corroborate the importance of the rG4 region to recognize molecules involved in miRNA biogenesis. Among the species analyzed in this study, the rG4 region was shown to be conserved in all of them, which can confirm the biological relevance of the rG4 region (Pickering et al., 2011). In fact, it has been previously reported that NCL is involved in miRNA biogenesis of microRNAs 15a and 16 (Pickering et al., 2011). Recently, a study developed by Koralewska et al. also demonstrated that G4s bind to human dicer and inhibit its activity (Koralewska et al., 2021). These results are of greatest importance because indicated that G4s can play an important role in the control of miRNA biogenesis.

Once *in silico* approaches demonstrated the relevance of the G4 structure in the biological context, we employed CD and ^{1}H NMR spectroscopy to deeply investigate the formation of the G4 structure by pre-miRNA-149. The results from ^{1}H NMR spectroscopy suggested the formation of the G4 structure and probably, heterogeneity in the G4 molecularity, as observed by the intense overlapped signals in the G4 imino proton region (10–12 ppm) (Živković et al., 2020). The existence of Watson-Crick and G4 resonances in the presence of K^+, suggests that the formation of the G4 in pre-miRNA-149 is locked by a stem structure (Miranda et al., 2021b).

The results obtained after addition of 100 mM KCl and annealing, revealed a slight shift of the positive band, which suggests a reorganization of the secondary structure. Moreover, the results obtained after cooling the solution at 4 °C for 24 h or 48 h showed that, after annealing the solution in each step, pre-miRNA-149 retains its ellipticity. In our work with the rG4 region (5′-GGGAGGGAGGGACGGG-3′), we demonstrated that the G4 structure is stable for 7 days without changes in the ellipticity signal intensity, even in the presence of a cellular medium, supplemented with 10% fetal bovine serum (Santos et al., 2019). The G4 formation is also dependent from K^+ concentration as highlighted by CD titrations and CD melting experiments.

The stabilization or destabilization through ligand binding is frequently used to maintain the folded state or to disrupt the G4 structure, respectively. Until now, some small molecules able to interact with G4 pre-miRNA-149 structure have been identified (Ghosh et al., 2019; Kwok et al., 2016; Santos et al., 2019). For instance, the well-known G4 ligand PDS was found to induce and stabilize the G4 structure (Kwok et al., 2016), while TMPyP4 was found to disrupt/aggregate the G4 structure (Ghosh et al., 2019). The destabilization of G4 structures by G4 ligands is less commonly described, but some examples have been reported in the last few years (Ghosh et al., 2019; Mitteaux et al., 2021; Morris et al., 2012; Zamiri et al., 2014). For instance, a study developed by Zamiri et al. described the disruption of the RNA G4 structures of the

disease-associated r(GGGGCC)n repeat of the C9orf72 gene (Zamiri et al., 2014). The disruption of those structures hinders the binding of proteins to the RNA G4 structures (Zamiri et al., 2014).

Acridine orange (C_8 and C_8—NH_2) and phenanthroline (PhenDC3) derivatives were previously described as G4 binders and stabilizers (Figueiredo et al., 2021; Santos et al., 2020, 2019). Upon addition of 2 molar equivalents, the CD melting results revealed a stabilizer effect of C_8 and C_8—NH_2 ligands and a destabilizer effect of PhenDC3. However, in the presence of 4 molar equivalents of C_8—NH_2, the melting temperature also decreased to 61.7 ± 0.5 °C (data not shown). The presence of the iodobenzene group at the end of the alkylamide chain seems to have a pronounced effect on the stability of the pre-miRNA-149. Moreover, at 2 molar equivalents, C_8 have the best stabilizer effect with two melting points. Comparable results were obtained by Arachchilage et al. for pre-miRNA-92b in the presence of 5 mM KCl (Mirihana Arachchilage et al., 2015). They observed two melting points attributed to the stem-loop and the G4 structures (Mirihana Arachchilage et al., 2015). In a previous report, we analyzed the rG4 region of pre-miRNA-92b (5′-GGGCGGGCGGGAGGG-3′) and observed two melting temperatures (Santos et al., 2020). We hypothesized that the two melting temperatures could be derived from multiple rG4 conformations with different degrees of stabilization.

Among G4 interacting proteins, NCL is the protein most often reported for its functions upon G4 recognition. It is generally believed that NCL preferentially recognizes G4 structures and helps stabilize them (Tosoni et al., 2015). Therefore, the proper folding of the G4 structure and its stability in the presence K^+ and ligands are fundamental issues for the successful recognition of NCL in the cellular context, whereas K^+ is known to be present in a concentration around 140–150 mM (Zacchia et al., 2016). Our results indicated that in the presence of K^+ concentrations higher than 50 mM, pre-miRNA-149 melting temperature surpasses 90 °C, which could significantly contribute to NCL recognition.

Molecular docking and molecular dynamics studies provided important structural insights on the binding of NCL RBD1,2 to the rG4 region of pre-miRNA-149 (5′-GGGAGGGAGGGACGGG- 3′). Recently, we have built the 3D model of rG4 region of pre-miRNA-149 and deeply investigated the interaction of the G4 structure found in pre-miRNA-149 with six distinct well-known G4 ligands. Among the ligands studied were C_8, C_8—NH_2 and PhenDC3. Here, we investigated the binding of NCL RBD1,2 to the parallel rG4 structure. The results revealed the binding of the rG4 structure to a cavity between domains 1 and 2. The atomic interaction mainly occurs by intermolecular hydrogen bonds and hydrophobic interactions. The results are similar to those reported by some of us with the rG4 region of pre-miRNA-92b (Santos et al., 2020). Previously, this binding pocket was also described as the preferential binding site of the NCL aptamer AS1411 and pre-ribosomal RNA (Fan et al., 2016; Johansson et al., 2004).

In order to evaluate the molecularity of pre-miRNA-149 in the presence of ligands and NCL RBD1,2, we performed PAGE experiments. The results agree with CD data and suggest a total binding of pre-miRNA-149 to NCL RBD1,2 in the presence of C_8 but a partial binding in the presence of C_8—NH_2 and PhenDC3.

One of the key parameters to measure the affinity between molecules in a given G4/ligand or G4/protein interaction is the dissociation constant (K_D). The K_D of ligands (C_8, C_8—NH_2 and PhenDC3) towards pre-miRNA-149 was in the micromolar range (10^{-5}–10^{-6} M), which is in agreement with previous reports of ligands targeting G4 structures (Sun et al., 2019). The affinity of NCL RBD1,2 towards pre-miRNA-149 or pre-miRNA-149/PhenDC3 was in the nanomolar range (10^{-10}), which suggests a powerful binding of NCL RBD1,2 to pre-miRNA-149. These results agree with K_D values previously reported for the interaction of AS1411 or AS1411 derivative sequences and NCL (Carvalho et al., 2019; Miranda et al., 2021b).

Taking into account the intrinsic features of pre-miRNA-149, its potential applicability for therapeutic and diagnostic purposes is of immense interest. Considering that cell surface NCL is overexpressed in

the surface of prostate cancer cells, PC3 (Tate et al., 2006), we have used this cell line to evaluate the co-localization of NCL and pre-miRNA-149 labeled with FITC. The results obtained from confocal microscopy studies showed co-localization of pre-miRNA-149 and NCL in the surface PC3 cells. Comparing these results with those previously reported for the rG4 region (5′-GGGAGGGAGGGACGGG-3), where the sequence also colocalizes with cell surface NCL (Santos et al., 2019), we hypothesized that NCL recognition by pre-miRNA-149 could occur through the rG4 region.

Finally, by covalently immobilizing the pre-miRNA-149 sequence in a microfluidic device, we have successfully captured NCL RBD1,2 in a concentration-dependent manner. The results revealed that even at lower protein concentrations (0.25 μM), pre-miRNA-149 was able to capture NCL RBD1,2. Furthermore, it is possible to observe that in the presence of PhenDC3 the fluorescence intensity of NCL RBD1,2 was lower compared to pre-miRNA-149 without stabilization of PhenDC3, indicating that PhenDC3 could compete with NCL RBD1,2 by the binding to pre-miRNA-149. Indeed, it has been previously described that an excess of PhenDC3 disrupts the interaction of NCL with G4s (Saha et al., 2020). Since pre-miRNA-149 sequence can form a stable and resistant parallel G4, its applicability as biosensing agent to recognize NCL in microfluidic devices is of utmost relevance considering the advantages of those systems. When compared to other methods to recognize and detect NCL, such as western blot and ELISA, the microfluidics platform based on pre-miRNA-149 offers several advantages such as, better stability and reproducibility, shorter assay time (minutes *vs* hours of incubation), lower cost (oligonucleotides are cheaper than antibodies), less manipulation and procedures required (easier modification and immobilization), and potential to detect multiple targets (Jolly et al., 2016; Song et al., 2012).

Compared to other previously described devices and methods for NCL recognition and detection (Chalfin et al., 2017; Li et al., 2016; Maremanda et al., 2015), our approach was able to detect NCL RBD1,2 in a range between 0.25–5 μM with a minimum increase in concentration of 0.25 μM. Li et al. described a microcantilever biosensor system able to detect nucleolin over the range from 10 nM to 250 nM, and with a detection limit of 1.0 nM (Li et al., 2016). Despite this, we believe that our findings based on pre-miRNA-149 can be used to detect NCL in more complex samples.

5. Conclusion

In summary, we characterized the formation of a G4 structure by pre-miRNA-149 and the ability to recognize and capture NCL RBD1,2. Firstly, we have demonstrated the formation of G4 in the presence K^+ ions using NMR and CD experiments. Then, we showed the capacity of C_8 to stabilize the pre-miRNA-149 G4 structure. The complex formation of pre-miRNA-149 G4 with ligands and NCL RBD1,2 was proved using polyacrylamide gel electrophoresis. Using SPR, we determined binding affinities of pre-miRNA-149 G4 towards ligands and NCL RBD1,2. In the presence of PhenDC3, the binding to NCL RBD1,2 remains in the same order of magnitude (10^{-10} M). Finally, a microfluidic approach was applied to detect NCL RBD1,2 labeled with FITC. The results showed that fluorescence intensity depended on the NCL RBD1,2 flowed through the microfluidic channel. Altogether, these results could pave the way for future applications of pre-miRNA-149 G4 as a biosensing agent to detect NCL in cancer.

CRediT authorship contribution statement

Tiago Santos: Conceptualization, Methodology, Investigation, Data curation, Writing – original draft, Writing – review & editing. **André Miranda:** Investigation. **Lionel Imbert:** Investigation, Writing – review & editing. **Andreia Jardim:** Investigation. **Catarina R.F. Caneira:** Investigation. **Virgínia Chu:** Resources. **João P. Conde:** Resources. **Maria Paula Cabral Campello:** Resources. **António Paulo:** Resources.

Gilmar Salgado: Data curation, Writing – review & editing. **Eurico J. Cabrita:** Data curation, Writing – review & editing. **Carla Cruz:** Conceptualization, Methodology, Supervision, Data curation, Resources, Funding acquisition, Investigation, Writing – review & editing.

Declaration of Competing Interest

There are no conflicts of interest to declare.

Acknowledgements

Supplementary materials

Supplementary material associated with this article can be found, in the online version, at doi:10.1016/j.ejps.2021.106093.

References

Bates, P.J., Reyes-Reyes, E.M., Malik, M.T., Murphy, E.M., O'Toole, M.G., Trent, J.O., 2017. G-quadruplex oligonucleotide AS1411 as a cancer-targeting agent: uses and mechanisms. Biochim. Biophys. Acta Gen. Subj. 1861, 1414–1428. https://doi.org/10.1016/j.bbagen.2016.12.015.

Beaudoin, J.D., Jodoin, R., Perreault, J.P., 2014. New scoring system to identify RNA G-quadruplex folding. Nucleic Acids Res.. 42, 1209–1223. https://doi.org/10.1093/nar/gkt904.

Berger, C.M., Gaume, X., Bouvet, P., 2015. The roles of nucleolin subcellular localization in cancer. Biochimie 113, 78–85. https://doi.org/10.1016/j.biochi.2015.03.023.

Brázda, V., Kolomazník, J., Lýsek, J., Bartas, M., Fojta, M., Šťastný, J., Mergny, J.L., 2019. G4Hunter web application: a web server for G-quadruplex prediction. Bioinformatics 35, 3493–3495. https://doi.org/10.1093/bioinformatics/btz087.

Carvalho, J., Paiva, A., Cabral Campello, M.P., Paulo, A., Mergny, J.-.L., Salgado, G.F., Queiroz, J.A., Cruz, C., 2019. Aptamer-based Targeted Delivery of a G-quadruplex Ligand in. Cervical Cancer Cells. Sci. Rep. 9, 7945. https://doi.org/10.1038/s41598-019-44388-9.

Carvalho, J., Santos, T., Carrilho, R., Sousa, F., Salgado, G.F., Queiroz, J.A., Cruz, C., 2020. Ligand screening to pre-miRNA 149 G-quadruplex investigated by molecular dynamics. J. Biomol. Struct. Dyn. 38, 2276–2286. https://doi.org/10.1080/07391102.2019.1632743.

Chalfin, H.J., Verdone, J.E., van der Toom, E.E., Glavaris, S., Gorin, M.A., Pienta, K.J., 2017. Nucleolin staining may aid in the identification of circulating prostate cancer cells. Clin. Genitourin. Cancer 15, e477–e481. https://doi.org/10.1016/j.clgc.2016.12.004.

Fan, X., Sun, L., Wu, Y., Zhang, L., Yang, Z., 2016. Bioactivity of 2′-deoxyinosine-incorporated aptamer AS1411. Sci. Rep. 6, 25799. https://doi.org/10.1038/srep25799.

Figueiredo, J., Miranda, A., Lopes-Nunes, J., Carvalho, J., Alexandre, D., Valente, S., Mergny, J.L., Cruz, C., 2021. Targeting nucleolin by RNA G-quadruplex-forming motif. Biochem. Pharmacol. 189, 114418 https://doi.org/10.1016/j.bcp.2021.114418.

Garant, J.M., Perreault, J.P., Scott, M.S., 2018. G4RNA screener web server: user focused interface for RNA G-quadruplex prediction. Biochimie 151, 115–118. https://doi.org/10.1016/j.biochi.2018.06.002.

Garant, J.M., Perreault, J.P., Scott, M.S., 2017. Motif independent identification of potential RNA G-quadruplexes by G4RNA screener. Bioinformatics 33, 3532–3537. https://doi.org/10.1093/bioinformatics/btx498.

Ghosh, A., Ekka, M.K., Tawani, A., Kumar, A., Chakraborty, D., Maiti, S., 2019. Restoration of miRNA-149 expression by TmPyP4 induced unfolding of quadruplex within its precursor. Biochemistry 58, 514–525. https://doi.org/10.1021/acs.biochem.8b00880.

He, Y., Yu, D., Zhu, L., Zhong, S., Zhao, J., Tang, J., 2018. miR-149 in human cancer: a systemic review. J. Cancer 9, 375–388. https://doi.org/10.7150/jca.21044.

Hovanessian, A.G., Puvion-Dutilleul, F., Nisole, S., Svab, J., Perret, E., Deng, J.S., Krust, B., 2000. The cell-surface-expressed nucleolin is associated with the actin cytoskeleton. Exp. Cell Res. 261, 312–328. https://doi.org/10.1006/excr.2000.5071.

Huang, G., Su, C., Wang, L., Fei, Y., Yang, J., 2021. The application of nucleic acid probe–based fluorescent sensing and imaging in cancer diagnosis and therapy. Front. Chem. 9, 410. https://doi.org/10.3389/fchem.2021.705458.

Imbert, L., Lenoir-Capello, R., Crublet, E., Vallet, A., Awad, R., Ayala, I., Juillan-Binard, C., Mayerhofer, H., Kerfah, R., Gans, P., Miclet, E., Boisbouvier, J., 2021. *In vitro* production of perdeuterated proteins in H2O for biomolecular NMR studies. Methods Mol. Biol. 127–149. https://doi.org/10.1007/978-1-0716-0892-0_8.

Jia, W., Yao, Z., Zhao, J., Guan, Q., Gao, L., 2017. New perspectives of physiological and pathological functions of nucleolin (NCL). Life Sci. 186, 1–10. https://doi.org/10.1016/j.lfs.2017.07.025.

Johansson, C., Finger, L.D., Trantirek, L., Mueller, T.D., Kim, S., Laird-Offringa, I.A., Feigon, J., 2004. Solution structure of the complex formed by the two N-terminal RNA-binding domains of nucleolin and a pre-rRNA target. J. Mol. Biol. https://doi.org/10.1016/j.jmb.2004.01.056.

Jolly, P., Damborsky, P., Madaboosi, N., Soares, R.R.G., Chu, V., Conde, J.P., Katrlik, J., Estrela, P., 2016. DNA aptamer-based sandwich microfluidic assays for dual quantification and multi-glycan profiling of cancer biomarkers. Biosens. Bioelectron. https://doi.org/10.1016/j.bios.2015.12.058.

Kharel, P., Becker, G., Tsvetkov, V., Ivanov, P., 2020. Properties and biological impact of RNA G-quadruplexes: from order to turmoil and back. Nucleic Acids Res. 48, 12534–12555. https://doi.org/10.1093/nar/gkaa1126.

Kikin, O., D'Antonio, L., Bagga, P.S., 2006. QGRS Mapper: a web-based server for predicting G-quadruplexes in nucleotide sequences. Nucleic Acids Res. 34, W676–W682. https://doi.org/10.1093/nar/gkl253.

Klimentova, E., Polacek, J., Simecek, P., Alexiou, P., 2020. PENGUINN: precise exploration of nuclear G-Quadruplexes using interpretable neural networks. Front. Genet. 11, 1287. https://doi.org/10.3389/fgene.2020.568546.

Koralewska, N., Szczepanska, A., Ciechanowska, K., Wojnicka, M., Pokornowska, M., Milewski, M.C., Gudanis, D., Baranowski, D., Nithin, C., Bujnicki, J.M., Gdaniec, Z., Figlerowicz, M., Kurzynska-Kokorniak, A., 2021. RNA and DNA G-quadruplexes bind to human dicer and inhibit its activity. Cell. Mol. Life Sci. 78, 3709–3724. https://doi.org/10.1007/s00018-021-03795-w.

Koutsioumpa, M., Papadimitriou, E., 2014. Cell surface nucleolin as a target for anti-cancer therapies. Recent Pat. Anticancer Drug Discov. 9, 137–152. https://doi.org/10.2174/1574892808666131119095953.

Kozomara, A., Griffiths-Jones, S., 2014. MiRBase: annotating high confidence microRNAs using deep sequencing data. Nucleic Acids Res. 42, D68–D73. https://doi.org/10.1093/nar/gkt1181.

Kwok, C.K., Sahakyan, A.B., Balasubramanian, S., 2016. Structural analysis using SHALiPE to reveal RNA G-Quadruplex formation in human precursor microRNA. Angew. Chem. Int. Ed. 55, 8958–8961. https://doi.org/10.1002/anie.201603562.

Li, H., Bai, X., Wang, N., Chen, X., Li, J., Zhang, Z., Tang, J., 2016. Aptamer-based microcantilever biosensor for ultrasensitive detection of tumor marker nucleolin. Talanta 146, 727–731. https://doi.org/10.1016/j.talanta.2015.06.034.

Liu, G., Du, W., Xu, H., Sun, Q., Tang, D., Zou, S., Zhang, Y., Ma, M., Zhang, G., Du, X., Ju, S., Cheng, W., Tian, Y., Fu, X., 2020. RNA G-quadruplex regulates microRNA-26a biogenesis and function. J. Hepatol. 73, 371–382. https://doi.org/10.1016/j.jhep.2020.02.032.

Maremanda, N.G., Roy, K., Kanwar, R.K., Shyamsundar, V., Ramshankar, V., Krishnamurthy, A., Krishnakumar, S., Kanwar, J.R., 2015. Quick chip assay using locked nucleic acid modified epithelial cell adhesion molecule and nucleolin aptamers for the capture of circulating tumor cells. Biomicrofluidics 9, 054110. https://doi.org/10.1063/1.4930983.

Miranda, A., Santos, T., Carvalho, J., Alexandre, D., Jardim, A., Caneira, C.R.F., Vaz, V., Pereira, B., Godinho, R., Brito, D., Chu, V., Conde, J.P., Cruz, C., 2021a. Aptamer-based approaches to detect nucleolin in prostate cancer. Talanta 226, 122037. https://doi.org/10.1016/j.talanta.2020.122037.

Miranda, A., Santos, T., Largy, E., Cruz, C., 2021b. Locking up the as1411 aptamer with a flanking duplex: towards an improved nucleolin-targeting. Pharmaceuticals 14, 1–20. https://doi.org/10.3390/ph14020121.

Mirihana Arachchilage, G., Dassanayake, A.C., Basu, S., 2015. A potassium ion-dependent RNA structural switch regulates human pre-miRNA 92b maturation. Chem. Biol. 22, 262–272. https://doi.org/10.1016/j.chembiol.2014.12.013.

Mitteaux, J., Lejault, P., Wojciechowski, F., Joubert, A., Boudon, J., Desbois, N., Gros, C. P., Hudson, R.H.E., Boulé, J.B., Granzhan, A., Monchaud, D., 2021. Identifying G-Quadruplex-DNA-disrupting small molecules. J. Am. Chem. Soc. 143, 12567–12577. https://doi.org/10.1021/jacs.1c04426.

Morris, M.J., Wingate, K.L., Silwal, J., Leeper, T.C., Basu, S., 2012. The porphyrin TmPyP4 unfolds the extremely stable G-quadruplex in MT3-MMP mRNA and alleviates its repressive effect to enhance translation in eukaryotic cells. Nucleic Acids Res. 40, 4137–4145. https://doi.org/10.1093/nar/gkr1308.

Pereira, E., Do Quental, L., Palma, E., Oliveira, M.C., Mendes, F., Raposinho, P., Correia, I., Lavrado, J., Di Maria, S., Belchior, A., Vaz, P., Santos, I., Paulo, A., 2017. Evaluation of acridine orange derivatives as DNA-targeted radiopharmaceuticals for auger therapy: influence of the radionuclide and distance to DNA. Sci. Rep. 7, 42544. https://doi.org/10.1038/srep42544.

Pickering, B.F., Yu, D., Van Dyke, M.W., 2011. Nucleolin protein interacts with microprocessor complex to affect biogenesis of microRNAs 15a and 16. J. Biol. Chem. 286, 44095–44103. https://doi.org/10.1074/jbc.M111.265439.

Pinto, I.F., Caneira, C.R.F., Soares, R.R.G., Madaboosi, N., Aires-Barros, M.R., Conde, J. P., Azevedo, A.M., Chu, V., 2017. The application of microbeads to microfluidic systems for enhanced detection and purification of biomolecules. Methods 116, 112–124. https://doi.org/10.1016/j.ymeth.2016.12.005.

Rosenberg, J.E., Bambury, R.M., Van Allen, E.M., Drabkin, H.A., Lara, P.N., Harzstark, A. L., Wagle, N., Figlin, R.A., Smith, G.W., Garraway, L.A., Choueiri, T., Erlandsson, F., Laber, D.A., 2014. A phase II trial of AS1411 (a novel nucleolin-targeted DNA aptamer) in metastatic renal cell carcinoma. Invest. New Drugs 32, 178–187. https://doi.org/10.1007/s10637-013-0045-6.

Saha, A., Duchambon, P., Masson, V., Loew, D., Bombard, S., Teulade-Fichou, M.P., 2020. Nucleolin discriminates drastically between long-loop and short-loop quadruplexes. Biochemistry 1261–1272. https://doi.org/10.1021/acs.biochem.9b01094.

Santos, T., Miranda, A., Campello, M.P.C., Paulo, A., Salgado, G., Cabrita, E.J., Cruz, C., 2020. Recognition of nucleolin through interaction with RNA G-quadruplex. Biochem. Pharmacol. 189, 114208 https://doi.org/10.1016/j.bcp.2020.114208.

Santos, T., Pereira, P., Campello, M.P.C., Paulo, A., Queiroz, J.A., Cabrita, E., Cruz, C., 2019. RNA G-quadruplex as supramolecular carrier for cancer-selective delivery. Eur. J. Pharm. Biopharm. 142, 473–479. https://doi.org/10.1016/j.ejpb.2019.07.017.

Santos, T., Salgado, G.F., Cabrita, E.J., Cruz, C., 2021. G-quadruplexes and their ligands: biophysical methods to unravel G-quadruplex/ligand interactions. Pharmaceuticals 14, 769. https://doi.org/10.3390/ph14080769.

Shen, Q., Zhu, H., Lei, Q., Chen, L., Yang, D., Sui, W., 2020. MicroRNA-149-3p inhibits cell proliferation by targeting AKT2 in oral squamous cell carcinoma. Mol. Med. Rep. 23, 172. https://doi.org/10.3892/MMR.2020.11811.

Song, K.M., Lee, S., Ban, C., 2012. Aptamers and their biological applications. Sensors 12, 612–631. https://doi.org/10.3390/s120100612.

Sun, H., Tan, W., Zu, Y., 2016. Aptamers: versatile molecular recognition probes for cancer detection. Analyst 141, 403–415. https://doi.org/10.1039/c5an01995h.

Sun, Z.Y., Wang, X.-.N., Cheng, S.-.Q., Su, X.-.X., Ou, T.-.M., 2019. Developing novel G-quadruplex ligands: from interaction with nucleic acids to interfering with nucleic acid⁻protein interaction. Molecules 24, 396. https://doi.org/10.3390/molecules24030396.

Tao, Y., Zheng, Y., Zhai, Q., Wei, D., 2021. Recent advances in the development of small molecules targeting RNA G-quadruplexes for drug discovery. Bioorg. Chem. 110, 104804 https://doi.org/10.1016/j.bioorg.2021.104804.

Tate, A., Isotani, S., Bradley, M.J., Sikes, R.A., Davis, R., Chung, L.W.K., Edlund, M., 2006. Met-independent Hepatocyte Growth Factor-mediated regulation of cell adhesion in human prostate cancer cells. BMC Cancer. https://doi.org/10.1186/1471-2407-6-197.

Tosoni, E., Frasson, I., Scalabrin, M., Perrone, R., Butovskaya, E., Nadai, M., Palù, G., Fabris, D., Richter, S.N., 2015. Nucleolin stabilizes G-quadruplex structures folded by the LTR promoter and silences HIV-1 viral transcription. Nucleic Acids Res. https://doi.org/10.1093/nar/gkv897.

Ugrinova, I., Petrova, M., Chalabi-Dchar, M., Bouvet, P., 2018. Multifaceted nucleolin protein and its molecular partners in oncogenesis. Advances in Protein Chemistry and Structural Biology, pp. 133–164. https://doi.org/10.1016/bs.apcsb.2017.08.001.

Yang, D., Du, G., Xu, A., Xi, X., Li, D., 2017. Expression of miR-149-3p inhibits proliferation, migration, and invasion of bladder cancer by targeting S100A4. Am. J. Cancer Res. 7, 2209–2219.

Zacchia, M., Abategiovanni, M.L., Stratigis, S., Capasso, G., 2016. Potassium: from physiology to clinical implications. Kidney Dis. 2, 72–79. https://doi.org/10.1159/000446268.

Zamiri, B., Reddy, K., Macgregor, R.B., Pearson, C.E., 2014. TMPyP4 porphyrin distorts RNA G-quadruplex structures of the disease-associated r(GGGGCC)n repeat of the C9orf72 gene and blocks interaction of RNA-binding proteins. J. Biol. Chem. 289, 4653–4659. https://doi.org/10.1074/jbc.C113.502336.

Živković, M.L., Rozman, J., Plavec, J., 2020. Structure of a DNA G-Quadruplex related to osteoporosis with a G-A bulge forming a pseudo-loop. Molecules 25, 4867. https://doi.org/10.3390/molecules25204867.